research papers

Conceptual design of a macromolecular neutron diffractometer (MaNDi) for the SNS

Arthur J. Schultz,[a]* P. Thiyagarajan,[a] Jason P. Hodges,[b,c] Christine Rehm,[b] Dean A. A. Myles,[d] Paul Langan[e] and Andrew D. Mesecar[f]

[a]Intense Pulsed Neutron Source, Argonne National Laboratory, IL 60439, USA, [b]Spallation Neutron Source, Oak Ridge National Laboratory, TN 37831, USA, [c]Metals and Ceramics Division, Oak Ridge National Laboratory, TN 37831, USA, [d]Center for Structural Molecular Biology, Oak Ridge National Laboratory, TN 37831, USA, [e]Biosciences Division, Los Alamos National Laboratory, NM 87545, USA, and [f]Center for Pharmaceutical Biotechnology, Department of Medicinal Chemistry and Pharmacognosy, University of Illinois at Chicago, IL 60607, USA. Correspondence e-mail: ajschultz@anl.gov

This paper describes the design criteria, calculations and simulations for a high-resolution macromolecular neutron diffractometer (MaNDi) for the Spallation Neutron Source (SNS). MaNDi is optimized to achieve 1.5 Å resolution from crystals of 0.1–1 mm^3 with lattice repeats in the range of 150 Å. It was determined that locating MaNDi on a decoupled hydrogen moderator beamline with a curved guide will provide data of higher resolution and higher signal-to-noise than a coupled hydrogen moderator at the SNS. In addition, for an instrument with an initial flight path of 24 m at the 60 Hz source and a wavelength bandwidth of $\Delta\lambda \simeq 2.7$ Å, bandwidth selection disk choppers can shift the wavelength range higher or lower for different experiments. With a wavelength range of 1.5–4.2 Å and $d_{min} = 2.0$ Å, simulations predict experiment duration times of 1–7 d, which is expected to revolutionize neutron macromolecular crystallography (NMC) for applications in the fields of structural biology, enzymology and computational chemistry.

1. Introduction

The construction of the Spallation Neutron Source (SNS) at Oak Ridge National Laboratory provides a unique opportunity for the development of a powerful high-resolution neutron diffractometer for structural biology. SNS will produce more than an order of magnitude higher intensity than existing pulsed spallation neutron facilities. A fully optimized diffractometer for neutron macromolecular crystallography (NMC) that also benefits from improved cryogenic moderators, state-of-the-art neutron guides, and high-sensitivity high-resolution detectors should provide additional factors for increased data rates and improved resolution.

NMC can play an important role in structural biology, enzymology and functional genomics because of its versatility in the accurate determination of protons, protonation states and hydration in macromolecular crystals, even at a moderate 2.0 Å resolution (Gutberlet et al., 2001; Tsyba & Bau, 2002; Niimura et al., 2003). Although ultra-high-resolution X-ray macromolecular crystallography (UHRXMC) on cryoprotected, highly ordered protein crystals at third-generation synchrotron sources can locate some of the more ordered H atoms (Longhi et al., 1997; Kuhn et al., 1998; Jelsch et al., 2000) and determine the protonation states of amino acid side chains

(Berisio et al., 1999), there are many instances where the information obtained remains inadequate. For instance, in myoglobin, even at resolutions better than 1.15 Å, UHRXMC did not provide adequate information on all of the H-atom positions (Kachalova et al., 1999; Vojtechovsky et al., 1999; Miele et al., 2003), while NMC on perdeuterated protein enabled more H-atom positions to be visualized in a structure determined to 2.0 Å resolution (Shu et al., 2000). The neutron structure to a resolution of 2.4 Å of the saccharide-binding protein concanavalin A revealed 62 D_2O molecules with both D atoms visible (Habash et al., 2000) as compared with 12 H_2O molecules from 0.94 Å X-ray data (Deacon et al., 1997). Recent neutron diffraction studies of deuterated human aldose reductase at 2.2 Å resolution revealed the location of the key proton that shuttles between Tyr48 and Lys77 during its enzymatic function (Podjarny et al., 2004). This H atom could not be identified from the X-ray structure alone, even with 0.66 Å resolution UHRXMC data (Ruiz et al., 2004). In addition, the enhanced visibility of (heavy) water D_2O molecules in neutron protein crystal structures allows precise details of solvent–protein interactions and of hydrogen-bonding networks and pathways to be mapped explicitly at the protein–solvent interface. Finally, owing to large differences in the scattering cross sections, NMC can discriminate between

neighboring metal atoms in the Periodic Table, such as Mn, Fe and Co, at the active sites of enzymes as well as in nucleic acids.

Even though NMC is a powerful technique, its productivity has been severely constrained by the scarcity and the intrinsic low brightness of available neutron sources. Currently there are only a very limited number of instruments that are useful for single-crystal macromolecular neutron crystallography: the Laue diffractometer LADI [Myles *et al.*, 1997; Kalb (Gilboa) *et al.*, 2001] at the Institut Laue–Langevin (ILL), Grenoble, France; the monochromatic diffractometer BIX3/BIX4 at the Japan Atomic Energy Research Institute (JAERI), Tokai (Tanaka *et al.*, 2002); and the time-of-flight Laue diffract-ometer at the Protein Crystallography Station (PCS) at Los Alamos National Laboratory (LANL) (Langan *et al.*, 2004). While the reactor-based LADI and BIX3 instruments have been operational for the past five to seven years, the time-of-flight diffractometer PCS at the spallation source at Los Alamos National Laboratory has become available only since late 2002. We note that in the context of the current world-wide interest in neutron protein crystallography there are plans to develop and extend instrument capabilities at current and future neutron facilities. These include the planned BIX-P1 instrument at the Japanese SNS and the development of the LADI-III instrument at the ILL, both of which will provide many-fold gains over existing instruments.

Here we describe the conceptual design for a dedicated high-resolution time-of-flight single-crystal macromolecular neutron diffractometer (MaNDi) at the SNS high-power target station (HPTS), which operates at 60 Hz. Design calculations, using analytical expressions and Monte Carlo simulations, show that the data rates at the MaNDi instrument can be one to two orders of magnitude greater than those of existing instruments. Thus, it should be possible to investigate larger unit-cell systems at high resolution using smaller crystals.

2. Conceptual design of MaNDi

MaNDi is designed for fast and efficient measurements of a full hemisphere of Bragg data with a resolution of 1.5 Å for macromolecular crystals with a volume of 0.1 mm^3 and with lattice constants in the range of 150 Å ($\Delta d/d = 1\%$). With larger crystals (> 1 mm^3), it will be possible to obtain useful data in the resolution range 2.0–2.5 Å for unit-cell repeats of up to 300 Å. A schematic model of MaNDi is shown in Fig. 1.

Employing well established analytical procedures and Monte Carlo simulations as described in §3, we have computed and compared the performance of MaNDi at both the coupled and the decoupled cryogenic liquid-hydrogen moderators and at both sides of the asymmetrically poisoned water moderators at the SNS. Over the most useful wavelength region of 1.5–5.0 Å for NMC, the coupled cryogenic liquid-hydrogen moderator produces a higher neutron flux than the decoupled cryogenic liquid-hydrogen moderator, which itself produces a higher flux than the water moderator. For the coupled moderator, however, the very high neutron flux is due to much

longer pulse widths, which significantly compromise the resolution for larger unit-cell systems. Our calculations show that the high-resolution applications in structural biology require a moderator that provides high neutron flux in the wavelength region 1.5–5 Å and narrow pulse widths, such as the decoupled liquid-hydrogen moderator at SNS. Furthermore, the improved signal-to-noise of the decoupled moderator leads to shorter data collection times than with the coupled moderator for medium to large unit cells with lattice constants of ~100 Å or greater (see §3).

On the basis of these evaluations, MaNDi has been designed for a decoupled hydrogen moderator with a 24.5 m flight path, allowing a wavelength bandwidth of about 2.69 Å (without any frame overlap) for the source frequency of 60 Hz at SNS. It will employ a set of three standard SNS choppers, located at 7.2, 8.2 and 10.4 m downstream from the moderator, for the selection of any wavelength range with $\Delta\lambda = 2.69$ Å in the 1–10 Å region. State-of-the-art high-index neutron supermirror guides will provide for efficient beam transport, leading to a flux gain at the sample position in the range 2–10 when compared with that with no guide. A curved guide in the middle section will also reduce the overall instrument background and will eliminate any potential radiation damage to the crystals by γ-rays and high-energy neutrons from the target. The combination of a wide wavelength bandwidth, sharp pulse widths at each wavelength and large solid-angle detector coverage will provide unprecedented high throughput and resolution for MaNDi in comparison with the current facilities for NMC. Thus, MaNDi will push the envelope in NMC on several fronts: high resolution and short data collection time with smaller crystals (< 1 mm^3 natural and ~0.1 mm^3 perdeuterated proteins) and unit-cell edges in the range 100–150 Å at 1.5–2 Å resolution.

Table 1 summarizes the preliminary instrument parameters of MaNDi, which will occupy a position next to the single-crystal diffractometer (Topaz, under construction at SNS beamline 12), sharing beam port 11 with the high-resolution powder diffractometer (POWGEN3).

2.1. Neutron guide system

To transport a wide wavelength range of cold neutrons from the moderator to the sample position efficiently, MaNDi will
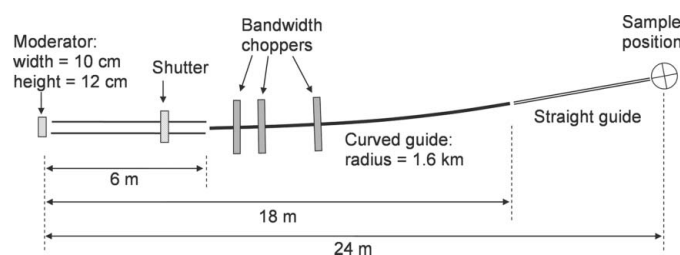
Figure 1
Top view of the layout of MaNDi. Distances along the beamline are approximately to scale. The curvature of the curved guide is highly exaggerated.

Table 1
Preliminary instrument parameters of MaNDi.

Moderator	Moderator type	Top upstream
	Material	Para-hydrogen
	Decoupler	Cadmium
	Poison	Gadolinium
	Poison depth	27 mm
	Width	0.10 m
	Height	0.12 m
Curved guide	Starting point	6 m downstream
	Width	1.5 cm
	Height	1.5 cm
	Length	12 m
	Supermirror coating	m = 3
	Total turn angle	0.43°
	Radius of curvature	1600 m
	Line-of-sight lost	∼20 m
Straight guide	Starting point	18 m downstream
	Width	1.5 cm
	Height	1.5 cm
	Length	Variable:
		3.0 m (FWHM = 0.23°, high resolution)
		4.5 m (FWHM = 0.38°, medium intensity)
		5.5 m (FWHM = 0.56°, high intensity)
	Supermirror coating	m = 3
Bandwidth disk choppers	Positions	7.2 m, 8.2 m, 10.4 m
Moderator-to-sample distance		24 m
Wavelength range		$\Delta\lambda$ = 2.69 Å
Wavelength resolution		∼0.15%
Sample-to-detector distance		0.3–0.5 m (to be determined later)
Detectors	Array of two-dimensional PSDs	1 mm resolution scintillation detectors

Figure 2
Ratio of the neutron flux at the sample position with and without the supermirror guide, as a function of wavelength (medium-intensity straight guide setting in Table 1).
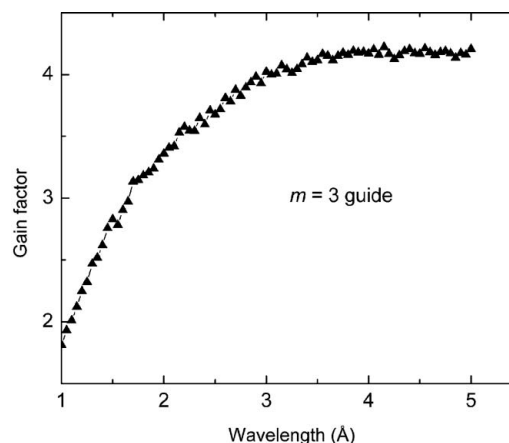
use high-index curved and straight supermirror guides because of the following advantages.

(i) Neutron guides offer significant gain in flux when compared with natural collimation with a view of the whole moderator.

(ii) Curved guides in the middle section of the beamline will steer the neutron beam such that the sample is completely out of the line-of-sight of the source. This will greatly reduce transport of any high-energy neutrons, and in so doing will reduce the background and eliminate the possibility of damage to the sample.

(iii) Small widths of the beam allow for the more efficient operation of bandwidth choppers for wavelength selection.

We performed Monte Carlo (MC) simulations using the *IDEAS* package (Lee & Wang, 2002) to optimize the length, location, curvature and choice of supermirror index coatings of the neutron guide system. MaNDi's guide system will start at a distance of 6 m from the moderator, and consists of a 12 m-long curved guide followed by a straight guide (Fig. 1), the length of which users can select on the basis of the resolution requirement. Thus, a guide that ends close to the sample will provide higher flux but also higher incident beam divergence, whereas a guide that ends further upstream will provide lower flux and lower beam divergence. The sample position is at 24 m and the distance between sample and detector will be

0.5 m or less. The sample-to-detector distance will be defined at a later stage giving due consideration to the spatial resolution of the detector, the cost, and the ΔQ resolution.

Fig. 2 shows that a substantial gain in neutron flux of up to a factor of four for the medium-intensity configuration (and a factor of about ten for the high-intensity configuration) at the sample position results from using a guide system (supermirror coating m = 3), when compared with the natural collimation. The intensity gain is directly related to the angular divergence of the beam as given in Table 1. However, experimenters can tune the incident neutron beam divergence to match the resolution requirements of a given experiment by using interchangeable sections of guide and/or a variety of collimators upstream to the sample position. Ideally, the incident divergence will match the mosaicity of the crystal to allow data collection to the highest resolution possible. In addition, the high-flux arrangement will be useful for partially ordered systems, such as fibers of biomacromolecules.

The moderator-to-detector length (24.5 m) of the instrument provides a large wavelength band of neutrons ($\Delta\lambda$ = 2.69 Å) that can be sorted by time-of-flight with a reasonable time resolution. Fig. 3 shows an MC simulation of neutron flux at the sample position (24 m downstream from the moderator). For the wavelength range of 1.1–3.8 Å ($\Delta\lambda$ = 2.7 Å), the integrated intensity is 6.9×10^7 n cm^{-2} s^{-1} for the high-intensity, 3.6×10^7 n cm^{-2} s^{-1} for the medium-intensity and 1.2×10^7 n cm^{-2} s^{-1} for the high-resolution guide setting. These intensities scale by the square of the ratios of the angular divergence (Table 1).

2.2. Beam-defining optics

The beam divergence can be readily tuned to experimental requirements by insertion of custom neutron optics, such as Soller collimators, polycapillary focusing optics (Gibson *et al.*, 2002; Mildner *et al.*, 2002), tapered guides and pinhole collimators, between the guide exit and the sample. It is fully recognized that the beam size should match the sample size in

Table 2
Available beamlines and the associated moderators at the SNS.

Moderator	Material	Decoupler	Poison	Poison depth	Beamline simulated	Beamline available
Top upstream	Para-hydrogen	Cadmium	Gadolinium	27 mm	11	11B
Top downstream	Para-hydrogen	None	None	n/a	5	14A
Bottom upstream	Water	Cadmium	Gadolinium	15 mm	8	8 or 9
Bottom upstream	Water	Cadmium	Gadolinium	25 mm	17	16
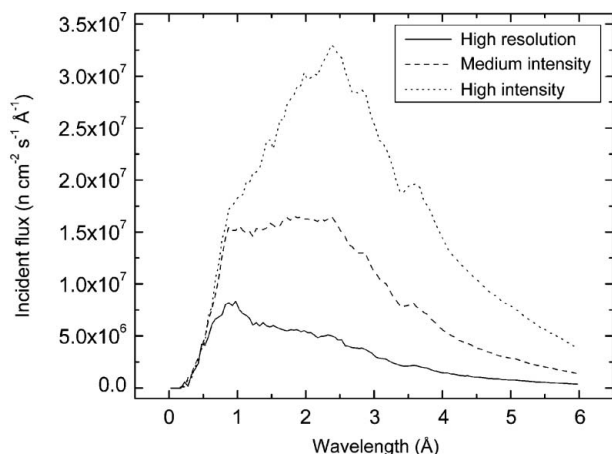
Figure 3
Monte Carlo simulations of the incident flux at the sample position for the three guide settings referred to in Table 1.

order to reach the maximum possible resolution and reduce the background.

2.3. Detectors

An array of state-of-the-art high-efficiency position-sensitive area detectors (PSDs) with a spatial resolution of ~1 mm will cover a wide solid angle around the sample. Both scintillator and gas detectors that meet the resolution and timing requirements for MaNDi are currently available. Recently developed scintillation detectors for the time-of-flight single-crystal neutron diffractometer SCD at the Intense Pulsed Neutron Source (De Lurgio & Naday, 2003) can potentially be used on MaNDi. Detectors under development at IPNS and at SNS will enable the use of tiled area detectors with minimal gaps. In addition, ^{3}He gas-filled multiwire detectors, such as the one in use on the PCS at Los Alamos (Langan et al., 2004), are possible candidates for MaNDi.

3. Choice of SNS moderator

The two conflicting parameters, intrinsic flux limitation and the high-resolution requirement (d_{min} = 1.5 Å, a = 150 Å) for structural biology, pose a challenge in the selection of the best moderator for NMC applications at SNS. It is important to note that at the SNS the positioning of the decoupled and coupled hydrogen moderators in the target–moderator system favors the decoupled moderator. Therefore, the flux gain factor for the coupled moderator when compared with the decoupled moderator is much less than that predicted for other spallation sources, such as JSNS at J-PARC, where the

coupled hydrogen moderator is in an optimal position. In the following we analyze the performances of a coupled hydrogen moderator, a decoupled hydrogen moderator and two sides of an asymmetrically poisoned decoupled water moderator for macromolecular diffraction applications at SNS, giving due consideration to resolution and counting statistics.

Because high-resolution structural biology requires a high flux of cold neutrons, some have proposed a coupled hydrogen moderator for NMC applications (Jauch, 1997; Wilson et al., 2001). However, at the SNS the increased flux from the coupled moderator (eight times that of the decoupled moderator at $\lambda > 2.5$ Å) comes at the cost of a pulse width that is about eight times longer than that of the decoupled moderator. Monte Carlo simulations show that if MaNDi views a coupled hydrogen moderator, the long tails in the emission times (pulse width) will be detrimental to both its ΔQ resolution and the counting statistics (signal-to-noise).

Table 2 provides a list of the moderators and beamlines for which 'metrics' and 'source' files are available (Iverson et al., 2002). These files contain the flux and pulse shape data that are used in the calculations and simulations. The decoupled hydrogen moderator refers to beamline 11 and the coupled hydrogen refers to beamline 5. We also performed Monte Carlo simulations for beamline 8 (high resolution) and beamline 17 (high intensity), which are on different sides of the decoupled water moderator. Table 2 also lists comparable beamlines that are currently not assigned to an instrument.

3.1. Effective flux of the decoupled hydrogen moderator

As the basis for decisions on the optimal wavelength range for the diffraction experiments, we define an effective flux calculated by weighting the flux from the moderator for the reflectivity of neutrons.

The integrated intensities I_{hkl} are related to structure-factor amplitudes $|F_{hkl}|$ based on the Laue formula (Buras & Gerward, 1975):

$$I_{hkl} = t\varphi(\lambda)A(\lambda)\left(\frac{V_s}{V_c}\right)\left(\frac{|F_{hkl}|^2}{V_c}\right)\frac{\lambda^4}{2\sin^2\theta}, \tag{1}$$

where t is the counting time, $\varphi(\lambda)$ is the incident neutron intensity per unit wavelength range at wavelength λ (n cm^{-2} s^{-1} Å^{-1}), $A(\lambda)$ is the sample absorption, V_s is the sample volume, V_c is the crystal unit-cell volume, F_{hkl} is the structure factor and θ is the Bragg angle.

Equation (1) can be rewritten as

$$I_{hkl} = t\varphi(\lambda)A(\lambda)N_s(|F_{hkl}|^2/V_c)\lambda^2(2d_{hkl}^2), \tag{2}$$

where N_s is the number of unit cells in the sample and d_{hkl} is the d spacing. The effective flux (Jauch, 1997; Wilson et al., 2001) is then

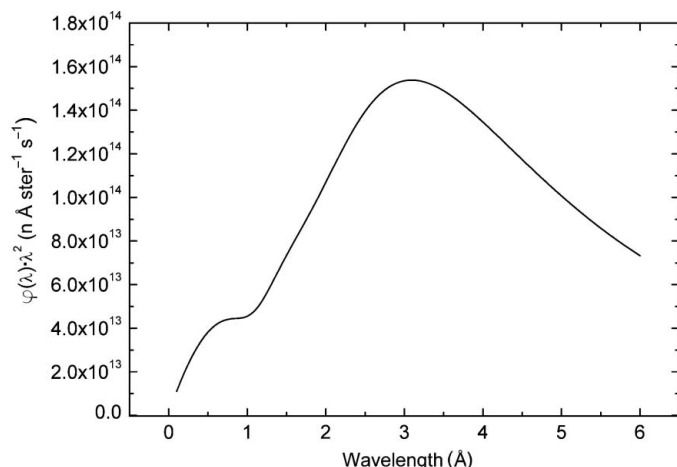$$\varphi_{\mathrm{eff}}(\lambda) = \varphi(\lambda)\lambda^2. \qquad (3)$$

In this case, one takes into account that for any hkl, the d spacing is constant regardless of the angle. Then, the optimal wavelength for measuring all Bragg peaks is the same, but the optimal angle will be different for each hkl.

Owing to the presence of statistical noise at the long wavelengths of simulated data in the moderator data files posted on the SNS web site (Iverson et al., 2002), we have used the parametric descriptions of Iverson et al. (2002) to obtain smoothed spectral curves. Multiplying the flux for the decoupled hydrogen moderator by λ^2 at each wavelength gives the curve shown in Fig. 4. It is clear from Fig. 4 that wavelengths in the range 2.0–5.0 Å provide the highest effective flux.

3.2. Comparison of flux from the liquid-hydrogen moderators

Fig. 5 shows the wavelength dependence of the ratios of the total intensity from the coupled and decoupled hydrogen moderators at the moderator surface. This is the gain in total intensity provided by the coupled hydrogen moderator. The figure indicates that for wavelengths of about 2.5 Å or greater a flux gain of eight can be obtained with the coupled moderator. However, the overall flux gain for the coupled moderator is much smaller in the important wavelength range of 1.5–2.5 Å.

We emphasize that the relative gains and pulse widths described in this paper are only applicable to the SNS moderator and target configuration. At the SNS the decoupled hydrogen moderator is at an advantageous location in the target–moderator system in order to provide more flux for high-resolution studies. At other sources, such as the Japanese J-PARC and the ISIS second target station, the configuration of the target–moderator system may be quite different, which may lead to different conclusions with regard to a coupled versus a decoupled moderator for NMC applications.

3.3. Resolution with different moderators

The resolution function for a time-of-flight powder or single-crystal diffractometer is frequently represented approximately as (Worlton et al., 1976)

$$R = \frac{\Delta Q}{Q} = \left[\left(\frac{\Delta t_{\mathrm{f}}}{t_{\mathrm{f}}}\right)^2 + \left(\frac{\Delta L}{L}\right)^2 + \left(\frac{1}{2}\Delta 2\theta \cot \theta\right)^2 \right]^{1/2}, \quad (4)$$

where $Q = 2\pi/d$, t_{f} is the time-of-flight, L is the total path length from moderator to detector, θ is the Bragg angle and the Δ terms are r.m.s. uncertainties. In terms of d spacings in real space, it can be shown that R also equals $\Delta d/d$.

Resolution in macromolecular crystallography refers to a minimum d spacing (d_{min}) to which observed data are obtained (Q_{max}), which is then also related to the ability to resolve features in the structure in real space. Let us consider the example of a cubic unit cell with a lattice spacing a. Then it can be shown that to resolve two Bragg peaks at d_{min}

$$R < d_{\mathrm{min}}/a. \qquad (5)$$

However, the resolution R as derived from equation (4) is based on a Gaussian distribution where the summed terms are standard deviations (σ). For single-crystal diffraction, it is not sufficient to resolve peaks, but we need to integrate the intensity under the peak such that peaks have to be fully separated. Therefore the resolution requirement is
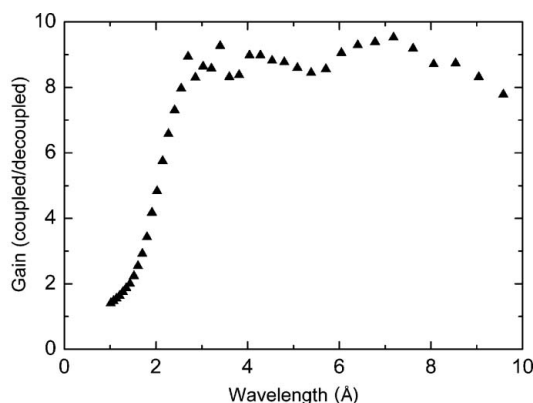
$$R < d_{\mathrm{min}}/5a, \qquad (6)$$

since from -2.5σ to 2.5σ about the mean contains almost 99% of a Gaussian peak (Jauch, 1986, 1993).

Since the Δ terms in equation (4) are often FWHM (full width at half-maximum) values and not standard deviations, where $5\sigma = 2.12$ FWHM, then

$$R_{\mathrm{FWHM}} < d_{\mathrm{min}}/2.12a. \qquad (7)$$

The pulse-width time resolution contributes primarily to the resolution parallel to the diffraction vector $\mathbf{Q}$, whereas the

Figure 4
Effective flux $\lambda^2\varphi(\lambda)$ versus wavelength at the moderator surface for the decoupled poisoned hydrogen moderator.
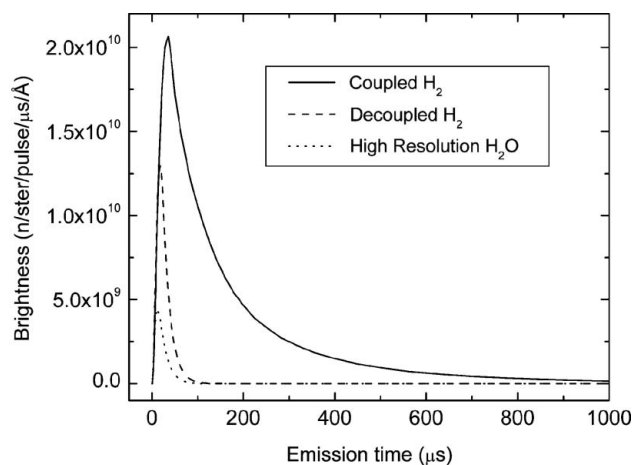

Figure 5
Intensity gain at the moderator surface of the coupled hydrogen moderator when compared with the decoupled moderator.

Table 3
Comparison of coupled and decoupled hydrogen moderators for the pulse corresponding to $\lambda = 2.55$ Å.

Parameter	Coupled H_2	Decoupled H_2	Ratio
Total intensity (n ster^{-1} s^{-1} Å^{-1})	1.82×10^{14}	2.28×10^{13}	8.0
FW at 90% of total intensity (µs)	430	45	9.6
FW at 10% of max (µs)	335	58	5.8

Figure 6
Pulse emission distribution for neutrons with $\lambda = 2.55$ Å at the moderator surfaces of the coupled and decoupled liquid-hydrogen moderators (and water) at SNS.

angular resolution primarily contributes to the direction perpendicular to the **Q** vector. From Jauch (1997), the condition

$$\Delta t_{\text{pulse}}(\text{FW}) \leq 505 L (d_{\text{min}}^2 / a) \sin\theta \qquad (8)$$

must be fulfilled for peaks to be completely separated in the direction of the reciprocal-lattice vector at d_{min} for a crystal with a unit-cell axis length of a. In this equation, the units are µs for t, m for L, and Å for d_{min} and a.

3.4. Effective FWHM of the pulses

Fig. 6 shows the pulse shapes for 2.55 Å neutrons from the coupled and decoupled hydrogen moderators. Pulse shapes for neutrons with other wavelengths are similar but depend in detail on the wavelengths. For the coupled liquid-hydrogen moderator, the intensity at the peak region of the pulse is only about 1.5 times greater than that from a decoupled liquid-hydrogen moderator. However, the pulse width is over eight times larger for the coupled moderator. Because the pulse shapes are asymmetric, not Gaussian, 2.12 FWHM does not contain 99% of the intensity under the peak. The values for the coupled and decoupled hydrogen moderators are compared in Table 3. Since 99% of the peak intensity is too stringent a condition, we have adopted a criterion to use a pulse length corresponding to 90% of the total intensity (integrating from $t = 0$), or a full width (FW) at 10% of the peak maximum, whichever is longer. It is seen from Table 3 that the eightfold gain in intensity with the coupled moderator comes about at the expense of nearly ten times larger pulse

Table 4
Calculated maximum allowed pulse full widths [derived from equation (8)] and ratios of the pulse full widths and intensities of the coupled and decoupled hydrogen moderators at different wavelengths for a 24.5 m instrument ($a = 150$ Å, $d_{\text{min}} = 1.5$ Å).

2θ (°)	λ (Å)	Equation (8) FW (µs)	Coupled FW (µs)	Decoupled FW (µs)	FW ratio	Intensity ratio
30	0.776	49	33	17	1.9	1.1
60	1.500	94	300	27	11.1	2.2
90	2.121	132	400	44	9.1	5.8
120	2.598	162	430	58	7.4	8.0
150	2.898	181	445	66	6.7	8.3

width than for the decoupled moderator. The longer pulse widths at the coupled moderator, in addition to affecting the resolution parallel to the **Q** vector, increase the background by about eight times, thus reducing the signal-to-noise ratio of the diffraction peaks, especially in the high-resolution shells. This is because only the one wavelength that Bragg scatters will contribute to the signal, whereas all wavelengths with pulse shape full widths that overlap with the Bragg wavelength pulse shape will contribute to the background.

Table 4 provides the maximum allowable pulse full widths derived from equation (8) for different wavelengths and corresponding Bragg angles to resolve peaks for a cubic system with $a = 150$ Å, $d_{\text{min}} = 1.5$ Å and $L = 24.5$ m. Also shown are the full widths corresponding to 90% of the total intensity, or 10% of the maximum, whichever is longer, for the pulse from each moderator.

The data in Table 4 lead to the following conclusions.

(*a*) The pulse width of the decoupled hydrogen moderator is better than adequate at all wavelengths. Perhaps a partially coupled moderator or one with a greater poison depth that can provide higher flux would be optimum, but such a moderator is not available at the SNS.

(*b*) The effective FW values for the coupled hydrogen moderator are higher than the values derived from equation (8) and hence a 24.5 m-long instrument cannot take advantage of the higher flux with the coupled moderator.

With regard to the coupled moderator, one way to take advantage of its higher flux is by increasing the length of the flight path to 75 m [see equation (8)]. However, there are several disadvantages of such a long flight path instrument.

(i) The usable wavelength bandwidth ($\Delta\lambda$) will be reduced by a factor of three because of the frame-overlap condition,

$$\Delta\lambda = 3955/(fL), \qquad (9)$$

where L is the instrument flight path length (m) and f is the source frequency (60 Hz at SNS).

(ii) As discussed in §3.7, resolution is still borderline when compared with the 24.5 m instrument viewing the decoupled hydrogen moderator.

(iii) Total guide efficiency for longer wavelengths at 75 m will be about 60% (based on MC simulations) and much less for shorter wavelengths.

(iv) There is a large additional cost associated with the construction of a 75 m-long instrument.

Table 5
Largest resolvable lattice constants at the peaks in the effective flux for water and decoupled hydrogen moderators, all else being equivalent.

	Water	Hydrogen
λ at peak in effective flux spectrum (Å)	1.25	3.10
2θ (°)	36	102
Resolution, $\Delta d/d$	0.011	0.0034
d_{min} (Å)	2.0	2.0
a, largest resolvable lattice constant at d_{min} (Å)	85	275
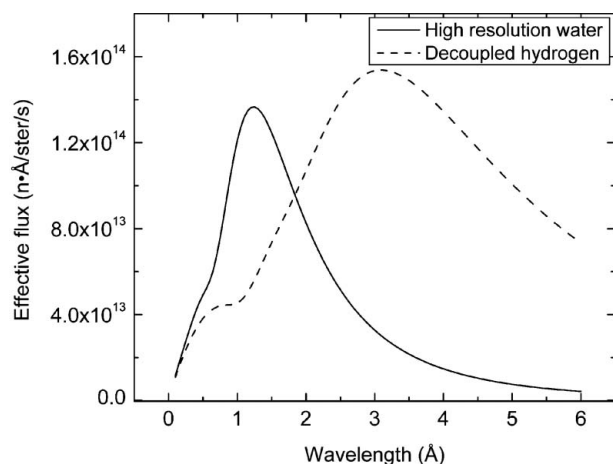
Figure 7
Effective flux at the moderator surface for the decoupled water (high-resolution side) and the decoupled hydrogen moderators at SNS.

3.5. Counting statistics

For protein crystals, the large unit cells lead to weak average peak intensities. In addition, there is a high background as a result of the large incoherent scattering of H atoms (unless the entire protein crystal is deuterated). For weak peaks with small signal-to-noise ratios, the standard deviation of an integrated peak $\sigma(I)$ based on counting statistics is essentially the square root of the background counts B (Wilkinson & Lehmann, 1991; Jauch, 1997; Wilson *et al.*, 2001).

In principle, if the peak widths are the same, increasing the integrated flux by a factor of eight in the case of the coupled moderator will increase the background by a similar factor such that

$$I_c/\sigma(I_c) = 8I_d/(8B_d)^{1/2} = 2.8I_d/\sigma(I_d), \qquad (10)$$

where I_c is the Bragg peak integrated intensity with the coupled hydrogen moderator and I_d is the intensity with the decoupled hydrogen moderator. Thus, there would appear to be an improvement by a factor of 2.8 in signal-to-noise ratio. This signal-to-noise gain is realizable only if the peak widths are the same, so that the number of points (time channels) that are sampled is identical. However, the effective pulse width for the coupled moderator (see Tables 3 and 4) is about eight times larger than that for the decoupled moderator, and hence sampling of that many more time channels would be required to determine the background properly. In equation (10), increasing the background counts B by another factor of eight

essentially cancels the effective increase in the signal due to a larger flux with the coupled moderator. However, for cases where $\sigma(I)$ is not principally dominated by the background, such as for large deuterated crystals with small unit cells, the coupled moderator could offer a modest advantage over the decoupled moderator, as discussed in §3.8.

3.6. Effective flux comparison for water and hydrogen moderators

For completeness, we also examined a comparison of the room-temperature water moderator with the cryogenic hydrogen moderator in terms of the effective flux [equation (3)]. Fig. 7 shows the effective flux calculated using the parametric descriptions of Iversen *et al.* (2002) and equation (3).

The maxima for the effective flux spectra of decoupled water and hydrogen moderators are at wavelengths of 1.25 and 3.10 Å, respectively. For a d spacing of 2.0 Å, the corresponding 2θ angles are 36 and 102°, respectively, as shown in Table 5. The resolution is according to equation (4).

The values in Table 5 indicate that, in the case of the water moderator, the maximum in effective flux can only be utilized efficiently with protein crystals of small unit-cell volume ($a \leq 85$ Å). For the decoupled hydrogen moderator, the maximum in effective flux coincides with the higher-resolution backscattering angles and hence can be utilized for protein crystal volumes ranging from small to large ($a \leq 275$ Å).

3.7. Resolution limits from Monte Carlo simulations

Monte Carlo simulations for a MaNDi instrument located on the four available beamlines were performed using the *IDEAS* program (Lee & Wang, 2002). Table 6 provides a summary of the protein crystal and beamline layout parameters for each of the instrument configurations simulated.

The medium-intensity guide setting configuration is appropriate for a wide range of protein unit-cell volumes and we use it here to compare the performance of a macromolecular diffractometer on each of the simulated beamlines. With the supermirror guide configuration set to medium-intensity mode, the incident neutron divergence is $\Omega = 0.38° \times 0.38°$ for $\lambda \geq 2.0$ Å. Fig. 8 shows a simulation of the transverse resolution for a typical set of outer-resolution-shell Bragg peaks ($d_{min} = 2$ Å) for a detector at $2\theta = 90°$ on beamline 11. The spatial widths of the Bragg peaks, all $\sim$7 mm, are close to that estimated from convoluting the neutron incident divergence (FW = 0.38°) with the crystal mosaicity (FW $\simeq$ 0.6°) and applying a sample–detector distance of 0.5 m, which yields an expected transverse peak width of 7.2 mm.

Monte Carlo simulations for each possible instrument configuration map the usable detector coverage (2θ range) as a function of unit-cell parameter, a, and outer-resolution-shell parameter, d_{min}. Such a usable coverage angle is shown in Fig. 9 for the medium-intensity guide system setting (see Table 6) for protein crystals with unit-cell parameters in the range $a = 75$–200 Å and an outer-resolution-shell requirement for resolving Bragg peaks of $d_{min} = 2$ Å. Note that for the diffractometer viewing the coupled hydrogen moderator, the

Table 6
Protein crystal parameters and the beamline layout parameters used in the MC simulations.

Protein crystal						
Mosaicity (FWHM, °)	0.2					
Strain (FWHM, %)	0.1					
Diameter (mm)	1.0					

Moderator (beamline)	Decoupled H_2 (11)		Coupled H_2 (5)		HR-H_2O (8), HI-H_2O (17)	
Beamline layout	High resolution	Medium intensity	High resolution	Medium intensity	High resolution	Medium intensity
Moderator–guide distance (m)	6.0	6.0	6.0	6.0	6.0	6.0
Curved guide section (m)	12.0	12.0	12.0	12.0	0.0	0.0
Straight guide section (m)	3.0	4.5	54.0†	55.5†	15.0	16.5
Guide–sample distance (m)	3.0	1.5	3.0	1.5	3.0	1.5
Sample–detector distance (m)	0.5	0.5	0.5	0.5	0.5	0.5
Moderator–sample distance (m)	24.0	24.0	75.0	75.0	24.0	24.0

Curved and straight guide sections are of 15 × 15 mm cross section except † where the straight guide section is of ballistic type (first and final 10 m are tapered, central ballistic section is of 25 × 25 mm cross section).
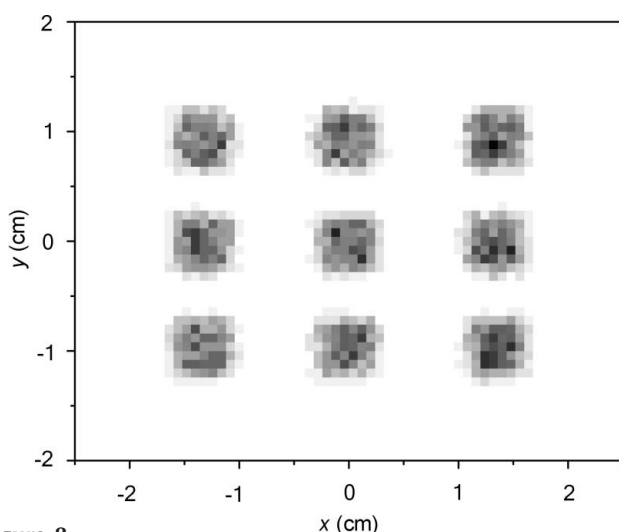
Figure 8
Simulated Bragg peaks at the detector plane calculated for SNS beamline 11 (decoupled hydrogen moderator) for a protein crystal with $a = 150$ Å for the medium-intensity straight guide configuration.
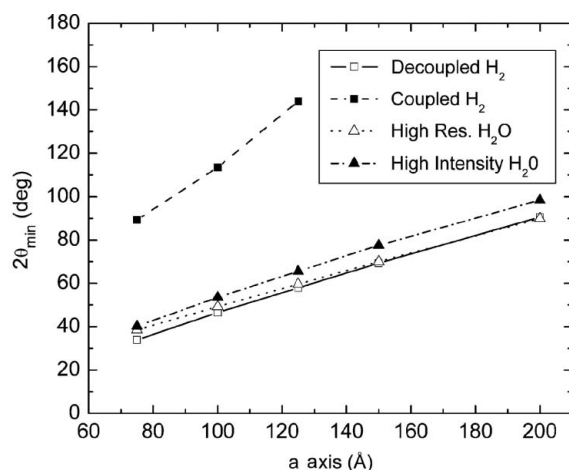
Figure 9
Minimum usable detector angle, $2\theta_{min}$, for resolvable Bragg peaks determined for MaNDi located on the comparison set of SNS beamlines. The Monte Carlo simulations were performed with the medium-intensity guide parameters for outer resolution shell $d_{min} = 2$ Å.

minimum 2θ value is about 105°, which limits the detector coverage and therefore increases the required number of crystal settings to obtain a complete set of data (see §3.8).

In order to confirm the resolution and pulse widths of peaks parallel to the Q vector, we simulated data similar to Fig. 8 but at a 2θ angle of 60°. Three orders of the peak centered at $d = 2.0$ Å ($Q = 2\pi/d = 3.14$ Å^{-1}) with a unit-cell repeat of 150 Å were simulated, corresponding to data obtained at different times-of-flight. Fig. 10 shows peak shapes for two different instrument configurations for the three peaks corresponding to the Bragg index $h = 74$, 75 and 76. It follows from Fig. 10 that using a 24.5 m-long instrument on a decoupled moderator would be the best choice for measuring a set of high-resolution Bragg data. Although a coupled moderator at 24.5 m (not shown) has higher flux, this extra intensity is not useful since it results in an increased background and peak width, resulting in overlapping peaks. Compared with a 24.5 m-long instrument for the coupled moderator, the 75.5 m-long instrument shows a better (but not complete) separation of the peaks.

The data in Fig. 10 completely agree with the results from the analytical calculations described earlier. If MaNDi views a coupled moderator, the instrument length would need to be more than 75 m in order to achieve a resolution similar to that of a 24.5 m-long instrument at a decoupled moderator. Moreover, on the basis of equation (9), the usable band width will decrease by a factor of three, thus losing some of the advantage of the higher flux with coupled moderator.

3.8. Data collection times

In order to evaluate all possible moderator options for a macromolecular diffractometer at the SNS, we carried out calculations of experiment beam times for the four moderators at the SNS (Table 2). Since perdeuterated macromolecular crystals provide an order of magnitude higher overall data rates when compared with the non-deuterated crystals (Shu *et al.*, 2000), we consider the case where most of the crystalline samples are deuterated and therefore the background is not primarily from incoherent scattering from H atoms.

Table 7
Parameters used for calculating the measurement time, t, per setting based on equations (1) and (11)–(13); flux and divergence parameters are from Monte Carlo simulations of the medium-intensity diffractometer configurations.

(a) Diffractometer parameters

	Dec-H_2 BL-11	Cou-H_2 BL-5	HR-H_2O BL-8	HI-H_2O BL-17
φ (n cm^{-2} s^{-1}Å^{-1})	1.30×10^7	7.17×10^7	3.69×10^6	7.09×10^6
Divergence (FWHM, °)	0.38	0.38	0.38	0.38
λ (Å)	2.83	2.83	2.83	2.83
2θ (°)	90	90	90	90
d_{min} (Å)	2.0	2.0	2.0	2.0
Total flight path (m)	24.5	75.5	24.5	24.5
TOF (µs)	17346	53453	17346	17346
Pulse width (FW) (µs)	71	447	56	80
$\Delta\lambda$ (Å)	0.0116	0.0237	0.0091	0.0130

(b) Crystal parameters for the case of a primitive cubic unit cell with $a = 150$ Å.

a (Å)	150
V_c (Å^3, unit-cell volume)	3.375×10^6
V_s (mm^3, crystal volume)	0.125
B (Å^2)	15
N_t (total of all atoms in unit cell)	375000
Fraction of C,N,O in protein	0.274
Fraction of H,D in protein	0.297
Fraction of O in water	0.143
Fraction of H,D in water	0.286
Fraction of ordered water molecules	0.65
Deuteration fraction	0.98
N_{ord} (all ordered atoms in unit cell)	318694
$\langle b^2 \rangle$ (cm^2, average b^2)	4.34×10^{-24}
Mosaic (°, FWHM)	0.2
σ_{inc}(H) (cm^2, ^{1}H incoherent cross section)	50×10^{-24}
$\Delta\Omega$ (rad^2)	0.0252

The average Bragg peak intensity at the minimum d spacing is evaluated using (1). Ignoring extinction effects, the average Bragg reflection at a particular $(\sin\theta)/\lambda$ is equal to the sum of the squares of the scattering factors times the Debye–Waller factor (Wilson, 1942), which for the neutron diffraction case is

$$\langle |F_{hkl}|^2 \rangle = \sum b_j^2 \exp(-2B \sin^2\theta/\lambda^2) = N_{ord}\langle b_j^2 \rangle T_{DW}, \quad (11)$$

where the summation is over the N_{ord} ordered atoms in the unit cell, $\langle b_j^2 \rangle$ is the average scattering length for all ordered atoms, and T_{DW} is the Debye–Waller factor. Using $\langle |F_{hkl}|^2 \rangle$ in (1) for the structure-factor amplitude, the average intensity $\langle I_{hkl} \rangle$ is calculated.

We evaluated the incoherent background counts due to hydrogen using the equation (Jauch, 1997)

$$B_{inc} = \varphi(\lambda)\Delta\lambda(V_s/V_c)\left(\sum \sigma_{inc}/4\pi\right)\Delta\Omega At, \quad (12)$$

where σ_{inc}(H) = 50 barns, σ_{inc}(D) = 2 barns and the summation is for all N_t atoms in the unit cell. The background due to diffuse coherent scattering was evaluated by

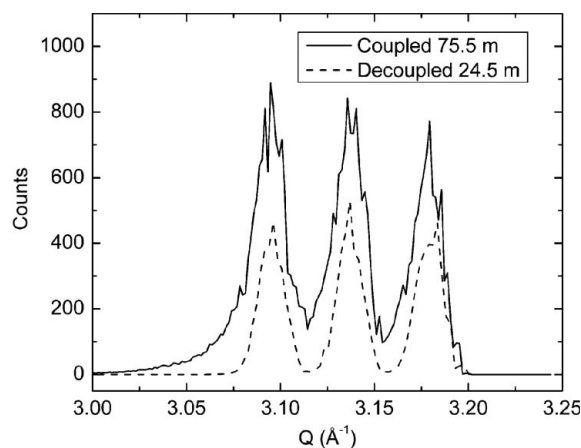$$B_{coh} = \varphi(\lambda)\Delta\lambda(V_s/V_c)\left[N_t(1 - T_{DW})\langle b_j^2 \rangle\right]\Delta\Omega At, \quad (13)$$

such that $B_{total} = B_{inc} + B_{coh}$. The counting time per setting was then calculated to achieve $I_{hkl}/\sigma(I_{hkl}) = 3$ at $d_{min} = 2$ Å, where $\sigma(I_{hkl}) = (I + 2B_{total})^{1/2}$. Table 7 summarizes the input to the

Table 8
Measurement time parameters t and D_{expt} (days) for a 98% perdeuterated protein crystal of volume 0.125 mm^3 and diffractometer located on the comparison set of SNS beamlines with the medium-intensity guide configuration.

		Diffractometer (moderator, beamline)			
a (Å)	Parameter	Dec-H_2 BL-11	Cou-H_2 BL-5	HR-H_2O BL-8	HI-H_2O BL-17
100	S	3	7	3	3
	t	0.32	0.09	1.02	0.62
	D_{expt}	1.0	0.6	3.1	1.9
125	S	3	24	3	3
	t	0.90	0.27	2.75	1.77
	D_{expt}	2.7	6.5	8.3	5.3
130	S	3	40	3	3
	t	1.08	0.33	3.30	2.15
	D_{expt}	3.2	13.2	9.9	6.5
150	S	3	–	3	3
	t	2.24	–	6.67	4.49
	D_{expt}	6.7	–	20.0	13.5

Figure 10
Peak shapes at $d_{min} = 2.0$ Å for a cubic unit cell of 150 Å for a diffractometer viewing the coupled hydrogen moderator with an initial flight path of 75.5 m, and for the decoupled hydrogen moderator with a flight path of 24.5 m.

above equations. The contents of a 'typical' protein crystal are based on an examination of the structural data for xylose isomerase at 0.86 Å resolution (Fenn *et al.*, 2004) provided in the PDB file 1muw. Table 8 gives the counting times per setting, t.

For the collection of a complete data set, which encompasses a hemisphere of reciprocal space out to resolution shell d_{min} of interest, the beam time required is

$$D_{expt} = St, \quad (14)$$

where S is the number of different crystal orientation settings and t is the measurement time for a single setting. The number of crystal settings, S, for a hemisphere of data can be evaluated from the expression

$$S = 1/(\sin\theta_{max} - \sin\theta_{min}), \qquad (15)$$

where $2\theta_{min}$ (see Fig. 9) and $2\theta_{max}$ are the minimum and maximum detector angles for which peaks can be resolved at d_{min}.[1] Here we use a $2\theta_{max}$ of 165°.
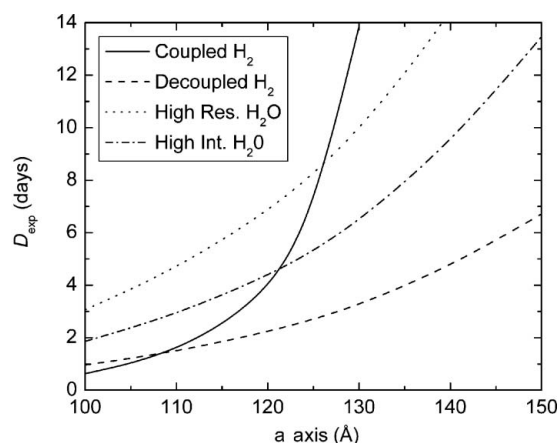
Using the above approach, we determined measurement times, t, at $2\theta = 90°$ for a single orientation for 98% perdeuterated protein crystals of unit-cell size $a = 100$–150 Å (a Debye–Waller parameter of $B_{iso} = 15$ Å^2 was used in the calculation of counting times). From the number of different crystal orientations, S, derived simply from usable detector coverage and rounded up to the nearest integer value, the experimental duration times, D_{expt}, for collecting a complete data set can be obtained. The number of settings for a full hemisphere based on equation (15) is used; there is not any reduction of the number of settings due to symmetry. A minimum value of $S = 3$ is adopted. The average time per crystal orientation and overall data collection time are given in Table 8.

Note that these results are based on counting times at $2\theta = 90°$. A more rigorous analysis of counting times as a function of 2θ gives similar results for the hydrogen moderators but significantly longer counting times for the water moderators. This difference is due to the decrease in the flux of the water moderators at the longer wavelengths that are utilized at higher scattering angles.

The calculated performance of the diffractometer for each moderator is best represented and assessed by a plot of estimated experiment duration *versus* protein unit-cell parameter, as shown in Fig. 11. Clearly, the performance of an instrument located on the decoupled cryogenic hydrogen-moderator beamline 11 is far superior to all the other candidate beamlines considered. Selecting a coupled cryogenic hydrogen beamline 5 would lead to the shortest measurement times for a single orientation for unit cells of $a < 130$ Å. However, this choice of moderator imposes broad Bragg peaks in time (poor longitudinal resolution) and reduced usable detector coverage. Consequently, the number of settings, S, will be large (see Table 8), which leads to D_{expt} for the full hemisphere of data becoming larger than that for the decoupled moderator.

The results indicate that for both the coupled and decoupled hydrogen moderators, experiment duration times for small unit cells are of the order of a day or two. For large unit cells, the decoupled moderator has a clear advantage since counting times can be a few days for the decoupled moderator versus a few weeks for the coupled moderator. Thus it is clear that the decoupled hydrogen moderator at SNS is the best choice for the MaNDi instrument.

For data to a resolution of 1.5 Å, data collection could be an order of magnitude longer for crystals in which the average B is reduced from 15 to 10 Å^3. Thus, cryocooling might be

---

[1] The surface area of the hemisphere of reflection is $2\pi R^2$, where $R = 1/d_{min}$. The surface area of a spherical cap bound by θ_{min} is $2\pi R^2(1 - \sin\theta_{min})$. Subtracting the area of the spherical cap for θ_{max} of less than 90° and dividing into the area of the hemisphere leads to $2\pi R^2/\{2\pi R^2[(1 - \sin\theta_{min}) - (1 - \sin\theta_{max})]\}$, which leads to equation (15).

Figure 11
Estimated experiment durations as a function of protein unit-cell parameter for a 98% perdeuterated protein crystal of volume 0.125 mm^3, $d_{min} = 2$ Å and a diffractometer located on the comparison set of SNS beamlines with high-intensity guide configuration.

necessary for samples with large unit cells ($a = 150$ Å, $V_c = 337\,500$ Å^3) in order to measure a complete data set with $d_{min} = 1.5$ Å.

4. Summary

NMC is able to determine accurate H-atom locations, protonation states and hydration, and hydrogen/deuterium exchange in macromolecular crystals even at a moderate 2 Å resolution. In order to exploit the high neutron flux that will become available beginning in 2006 at the Spallation Neutron Source, it is proposed to develop a dedicated high-throughput and high-resolution time-of-flight single-crystal macromolecular neutron diffractometer (MaNDi) at the SNS. MaNDi is being designed to be able to collect a full hemisphere of Bragg data with a resolution of 2 Å on a crystal with a lattice constant up to 150 Å in a few days. A thorough evaluation of the instrument performance at different moderators using analytical equations and Monte Carlo simulations shows that the decoupled hydrogen moderator at SNS would be the best choice for MaNDi. State-of-the-art neutron guides and optics provide for efficient beam transport and optimization of collimation at the sample. To reduce the radiation damage and the instrument background, a curved guide will be used to steer the beam so that the crystal will be out of line-of-sight of the moderator. The high throughput is accomplished by the use of a wide bandwidth of cold neutrons ($1.5 < \lambda < 4.2$ Å) sorted by time-of-flight and by an array of high-resolution position-sensitive area detectors covering a large solid angle. It is expected that the unprecedented high data rates and resolution with MaNDi for the high-resolution NMC will open up new avenues and greatly advance the field of structural biology, enzymology and computational chemistry.

research papers

References

Berisio, R., Lamzin, V. S., Sica, F., Wilson, K. S., Zagari, A. & Mazzarella, L. (1999). *J. Mol. Biol.* **292**, 845–854.

Buras, B. & Gerward, L. (1975). *Acta Cryst.* A**31**, 372–374.

Deacon, A., Gleichmann, T., Kalb (Gilboa), A. J., Price, H., Raftery, J., Bradbrook, G., Yariv, J. & Helliwell, J. R. (1997). *J. Chem. Soc. Faraday Trans.* **93**, 4305.

De Lurgio, P. M. & Naday, I. (2003). Annual Meeting of the American Crystallographic Association, Cincinnati, Ohio, American Crystallographic Association, Abstract No. W0185.

Fenn, T. D., Ringe, D. & Petsko, G. A. (2004). *Biochemistry*, **43**, 6464–6474.

Gibson, W. M., Schultz, A. J., Chen-Mayer, H. H., Mildner, D. F. R., Gnäupel-Herold, T., Miller, M. E., Prask, H. J., Vitt, R., Youngman, R. & Carpenter, J. M. (2002). *J. Appl. Cryst.* **35**, 677–683.

Gutberlet, T., Heinemann, U. & Steiner, M. (2001). *Acta Cryst.* D**57**, 349–354.

Habash, J., Raftery, J., Nuttall, R., Price, H. J., Wilkinson, C., Kalb, A. J. & Helliwell, J. R. (2000). *Acta Cryst.* D**56**, 541–550.

Iverson, E. B., Ferguson, P. D., Gallmeier, F. X. & Popova, I. I. (2002). *Detailed SNS Neutronics Calculations for Scattering Instrument Design: SCT Configuration*. SNS Technical Document 110040300-DA0001-R00, Oak Ridge National Laboratory, TN, USA. http://www.sns.gov/users/instrument_systems/components/moderator/.

Jauch, W. (1986). ISIS Workshop, Rapallo, Italy.

Jauch, W. (1993). *Trans. Am. Crystallogr. Assoc.* **29**, 55–61.

Jauch, W. (1997). *J. Neutron Res.* **6**, 161–171.

Jelsch, C., Teeter, M. M., Lamzin, V., Pichon-Pesme, V., Blessing, R. H. & Lecomte, C. (2000). *Proc. Natl Acad. Sci. USA*, **97**, 3171–3176.

Kachalova, G. S., Popov, A. N. & Bartunik, H. D. (1999). *Science*, **284**, 473–476.

Kalb (Gilboa), A. J., Myles, D. A. A., Habash, J., Raftery, J. & Helliwell, J. R. (2001). *J. Appl. Cryst.* **34**, 454–457.

Kuhn, P., Knapp, M., Soltis, S. M., Ganshaw, G., Thoene, M. & Bott, R. (1998). *Biochemistry*, **37**, 13446–13452.

Langan, P., Greene, G. & Schoenborn, B. P. (2004). *J. Appl. Cryst.* **37**, 24–31.

Lee, W.-T. & Wang, X.-L. (2002). *Neutron News*, **13**, 30–34.

Longhi, S., Czjzek, M., Lamzin, V., Nicolas, A. & Cambillau, C. (1997). *J. Mol. Biol.* **268**, 779–799.

Miele, A. E., Federici, L., Sciara, G., Draghi, F., Brunori, M. & Vallone, B. (2003). *Acta Cryst.* D**59**, 982–988.

Mildner, D. F. R., Chen-Mayer, H. H., Gibson, W. M., Gnäupel-Herold, T., Miller, M. E., Prask, H. J., Schultz, A. J., Vitt, R. & Youngman, R. (2002). *Rev. Sci. Instrum.* **73**, 1985–1993.

Myles, D. A. A., Bon, C., Langan, P., Cipriani, F., Castagna, J. C., Lehmann, M. S. & Wilkinson, C. (1997). *Physica B Condens. Matter*, **241**, 1122–1130.

Niimura, N., Chatake, T., Ostermann, A., Kurihara, K. & Tanaka, I. (2003). *Z. Kristallogr.* **218**, 96–107.

Podjarny, A., Mitschler, A., Hazemann, I., Blakeley, M., Dauvergne, M. T., Meilleur, F., Van Zandt, M., Ginell, S., Joachimiak, A. & Myles, D. (2004). Annual Meeting of the American Crystallographic Association, Chicago, American Crystallographic Association, Abstract No. W0159.

Ruiz, F., Hazemann, I., Mitschler, A., Joachimiak, A., Schneider, T., Karplus, M. & Podjarny, A. (2004). *Acta Cryst.* D**60**, 1347–1354.

Shu, F., Ramakrishnan, V. & Schoenborn, B. P. (2000). *Proc. Natl Acad. Sci. USA*, **97**, 3872–3877.

Tanaka, I., Kurihara, K., Chatake, T. & Niimura, N. (2002). *J. Appl. Cryst.* **35**, 34–40.

Tsyba, I. & Bau, R. (2002). *Chemtracts – Inorg. Chem.* **15**, 233–257.

Vojtechovsky, J., Chu, K., Berendzen, J., Sweet, R. M. & Schlichting, I. (1999). *Biophys. J.* **77**, 2153–2174.

Wilkinson, C. & Lehmann, M. S. (1991). *Nucl. Instrum. Methods A*, **310**, 411–415.

Wilson, A. J. C. (1942). *Nature (London)*, **150**, 151–152.

Wilson, C. C., Jauch, W., McIntyre, G. J., Myles, D. A. A. & Peters, J. (2001). *Report of the ESS Instrumentation Task Group: Single Crystal Diffraction Working Group for the ESS SAC Workshop in May 2001*, edited by F. Mezei, R. S. Eccleston & T. Gutberlet, pp. 33–40. Jülich, Germany: The ESS Project.

Worlton, T. G., Jorgensen, J. D., Beyerlein, R. A. & Decker, D. L. (1976). *Nucl. Instrum. Methods*, **137**, 331–337.